An Integrated Simulation of Multiple-Pass U-10Mo Alloy Hot Rolling and Static Recrystallization

WILLIAM E. FRAZIER, KARUN KALIA, CHAO WANG, KYOO SIL CHOI, DAVID P. FIELD, SHENYANG HU, AYOUB SOULAMI, and VINEET V. JOSHI

To achieve a desired microstructure and minimize the thickness variation in rolled foils, researchers must understand the effects of foil fabrication process variables on microstructure evolution. We developed an integrated simulation of deformation and recrystallization that employs the finite element method (FEM) and the kinetic Monte Carlo (KMC) Potts model, respectively, to investigate microstructure evolution during multiple-pass hot rolling and heat treatment in polycrystalline U-10Mo fuel. Scanning electron microscopy and electron backscatter diffraction images of microstructures were directly used as input in FEM calculation of deformation, and the calculated strains were used to determine the driving force of nucleation and growth of recrystallized grains in the Potts model. Grain structures predicted by the Potts model were used to update the grain structure and material properties for FEM. Simulation alternated between FEM and the Potts model to simulate grain structure evolution during multiple rolling and heat treatments. The initial model parameters were determined by benchmarking the recrystallization kinetics against experimental data. Then, the model was applied to predict the grain structure evolution. Results showed that our model can capture the coupling between deformation and recrystallization and can quantitatively reproduce the observed U-10Mo recrystallization and grain growth kinetics. The simulation results demonstrated that the developed model can predict U-10Mo grain structures as a function of initial microstructure and foil fabrication parameters.

I. INTRODUCTION

THE alloy U-10Mo is a candidate low-enriched uranium fuel for experimental reactors.[1] The alloy has high U-density, thermal conductivity, and irradiation resistance, and can be easily rolled into a monolithic fuel foil.[1,2] The effect of the U-10Mo processing schedule on the fabricated fuel microstructure has been the subject of experimental and computational study, specifically for the purpose of improving fuel performance under irradiation.[3–6] It is believed that the grain structure of the fabricated fuel has a significant effect on radiation-induced recrystallization and swelling kinetics. Simulation efforts have predicted the effects of grain morphologies (grain size and aspect ratio) on recrystallization and swelling kinetics.[4,5,7] To achieve desired grain structures, it is therefore important to understand the effects of U-10Mo foil fabrication process variables on microstructure evolution. These variables constitute casting, homogenization, hot rolling, cold rolling, annealing, and a final hot isostatic press to bond the fuel foil to an Al cladding.[1] Depending upon the initial volume fraction of impurities and the homogenization heat treatment, a large variation in grain size prior to the rolling has been observed. This eventually affects the grain structure and the thickness variation of the rolled foil.[8,9] Second-phase particles such as uranium carbide (UC) and Mo–Si–U–C quaternary compounds are also present in U-10Mo alloys.[10] Experiments show that large, stiff particles play an important role in recrystallization and texture formation during rolling and annealing treatments.[11,12] This phenomenon is known as particle-stimulated nucleation (PSN).[13,14] The extent and effects of PSN depend on a number of factors, such as the particle size distribution, particle morphology, applied deformation, and strain rate.[1,13,15–17]

WILLIAM E. FRAZIER, KYOO SIL CHOI, SHENYANG HU, AYOUB SOULAMI, and VINEET V. JOSHI are with the Pacific Northwest National Laboratory, P. O. Box 999, Richland, WA 99354. Contact e-mail: william.frazier@pnnl.gov KARUN KALIA is with the University of Massachusetts, Lowell, MA. CHAO WANG is with the Pacific Northwest National Laboratory and also with the Framatome, 2101 Horn Rapids Rd, Richland, WA 99354. DAVID P. FIELD is with the Washington State University, Pullman, WA 99164.
CHAO WANG contributed work while at Pacific Northwest National Laboratory.

Therefore, rolling and annealing are expected to have the most significant effects on the final grain structure. Computational approaches to this multifaceted problem are an economically attractive alternative to a completely experimental analysis.

Researchers have recently developed several approaches for simulating deformation and annealing responses. The material systems modeled have included steels[18–22] copper,[23] magnesium alloys,[24] aluminum alloys,[25–28] α-uranium,[29] and even ice.[30] These models either generate the initial deformed microstructure through simulation or capture the initial state from micrographs.[22,25,29] Each approach has advantages and disadvantages. For example, some experimental methods can produce maps of dislocation density for a microstructure for use in simulation. These methods include the use of electron backscattered diffraction (EBSD),[25,26,29] synchrotron X-ray,[31–33] and transmission electron microscopy techniques.[34,35] However, these methods primarily measure the density of geometrically necessary dislocations, which can be calculated from measurement of the kernel average misorientation (KAM).[36] Methods such as high-resolution digital image correlation can produce strain maps with resolution on the order of tenths of micrometers,[37] and etching routines combined with computer image analysis can estimate dislocation density with similar resolution.[38,39] However, these methods can only provide mapping for the first stage of deformation, which is insufficient when multiple deformation and annealing steps need to be simulated. Crystal plasticity models used in conjunction with other models are well equipped to predict behaviors such as dynamic recrystallization,[21,23,40,41] texture development,[21] dislocation density, grain rotation,[42] the plastic and elastic contributions to the energy of deformation, and fracture.[43] This provides the advantage of evaluating the effects of these factors on recrystallization individually, such as the contributions of specific slip systems. These benefits come at an increased computational cost. A simple finite element method (FEM) approach can predict the accumulation of strain in a material, and similar models provide excellent insight into the development of the dislocation density.[21,27,30,44] An FEM Taylor–Bishop–Hill model can compute the spatial accumulation of strain for a polycrystalline grain structure, while accounting for spatial displacement effects and fracture.[45–47] This method was previously used by Cheng et al. to investigate the effect of particles in the U-10Mo microstructure on the formation of particle stringers, as well as the expected recrystallized microstructure.[48] Numerous approaches are available for simulating recrystallization response. A popular approach, the phase field method, can accommodate spatial deformation to the microstructure such as stretching,[44] but is generally limited in the number of available elements unless highly parallelized.[49] Further, phase field models, like other methods such as cellular automata and level-set approaches, generally must assume a specific criterion for recrystallization nucleation and then assume that the nucleation occurs at a specified rate.[21,50,51] However, the Monte Carlo Potts model can simulate recrystallization and grain growth efficiently in serial implementations while accommodating thousands of grains.[27,52,53] Recrystallization and grain growth events occur stochastically. Further, since interfaces are assumed to be atomically sharp in the Potts model, less computational power is required, and grains are easy to segment. While it is generally difficult to introduce dimensional changes in Potts model simulation without removing the simulation lattice entirely,[54] it is relatively simple to convert an FEM mesh to a lattice.[55] Therefore, as long as dynamic recrystallization is not extensive, an FEM–Potts model coupling should accurately simulate static recrystallization of a deformed alloy.

Our work employs FEM and the kinetic Monte Carlo (KMC) Potts model to describe an integrated simulation of deformation and recrystallization, respectively. Experimental parameters obtained from previous work allow us to determine the deformation, recrystallization, and grain growth responses of U-10Mo to hot rolling and subsequent annealing treatments between 600 °C and 700 °C, temperatures reasonably above the α-U solvus temperature.[56] Experimental observations of U-10Mo recrystallization over several rolling and annealing passes will allow us to confirm that our method can simulate multiple annealing passes. By doing this, we will demonstrate that our model can predict recrystallization behavior as a function of the parameter space of deformation treatment, annealing temperature, annealing duration, and initial microstructure.

II. METHODS

A. FEM Simulation of Rolling

In this study, a two-dimensional (2-D) plane strain compression model was adopted to simulate rolling of U-10Mo, because the deformations are predominantly along the rolling and normal directions in rolled materials, while there is very little deformation along the transverse direction. This simplified 2-D compression model is intended to capture the material deformation, especially in the central region of the sheet.

The microstructure-based FE model was generated based on an actual EBSD microstructure image. The image was mapped into the FE model such that each pixel of the image was treated as a single finite element. More specifically, for a given multiple-grain microstructure image, an in-house MATLAB code was implemented to assign the grain identification (ID), locate second-phase particles, convert each image pixel to the associated element number, and calculate the location of each pixel at a given scale. All of this information serve as input for the FE model.

Figure 1 shows the FE model generated based on an EBSD image. As shown in the figure, grains are presented using different colors and particles are shown in black. A four-node plane strain element with reduced integration (CPE4R in the commercial FEM software Abaqus/Explicit) was used in the model and its size was
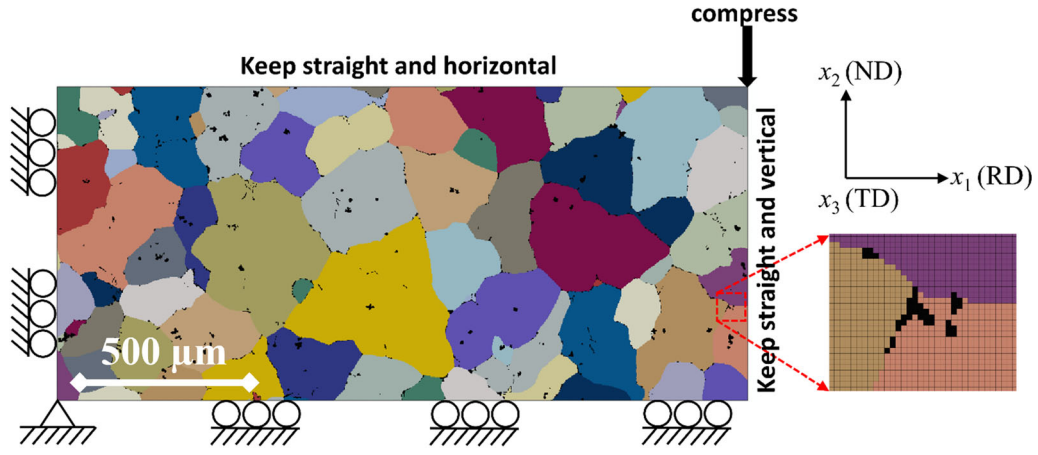
Fig. 1—Schematic of actual microstructure-based, plane strain, compression FEM model that simulates rolling of U-10Mo alloy. Simulations are performed on 2-D microstructures representing longitudinal cross sections of the U-10Mo fuel foils. RD, ND, and TD are rolling, normal, and transverse directions, respectively.

2×2 μm^2. Boundary conditions adopted in the model are also presented in the figure. Compression deformation is applied to the right-top corner of the model by displacement control. The top and right edges are kept straight horizontally and vertically, respectively, by multipoint constraint during deformation, and the left and bottom edges are also kept straight as shown in the figure. Note again that this modeling method can accurately represent the rolling deformation behavior in the center of sheet.

In the model, the second-phase particles were considered isotropic material subject to pure elastic deformation. The associated Young's modulus and Poisson's ratio are defined as 224.9 GPa and 0.288, respectively.[57] Our previous study[47] did not consider the actual polycrystal structure; it simplified the U-10Mo matrix as one isotropic material with ideal plasticity. In this study, we accounted for the polycrystalline grain structure and its anisotropic effect (due to different grain orientations) on the stress/strain fields by assigning an independent flow curve to each grain.[58] Each flow curve was devised to best mimic actual U-10Mo fuel microstructural behavior. As a result, the plastic behavior of each grain is assigned by an independent flow curve with a random $\pm$ 50 pct stress deviation from the baseline value to represent the degree of grain anisotropy.[59] The baseline stress and strain curve can be found in Hu *et al.*[47] Figure 2 shows the baseline flow curve of U-10Mo matrix material at 650 °C, and upper/lower bounds (*i.e.*, $\pm$ 50 pct) of random flow curves assigned to the multiple-grain model shown in Figure 1. The effect of work hardening disappears as strain exceeds 0.05. The elastic behavior of U-10Mo was characterized by a 65 GPa Young's modulus and 0.35 Poisson's ratio.[60] During rolling simulation, it is assumed that the deformation occurs with no cracking or fracturing. The simulations were performed using Abaqus/Explicit. The constitutive equation used here is

$$\mathrm{d}\sigma_{ij} = C_{ijkl}\mathrm{d}\varepsilon_{kl}^{e} = C_{ijkl}\big(\mathrm{d}\varepsilon_{kl} - \mathrm{d}\varepsilon_{kl}^{p}\big), \qquad [1]$$

where $\mathrm{d}\sigma_{ij}$ is stress increment, C_{ijkl} is the elastic tensor
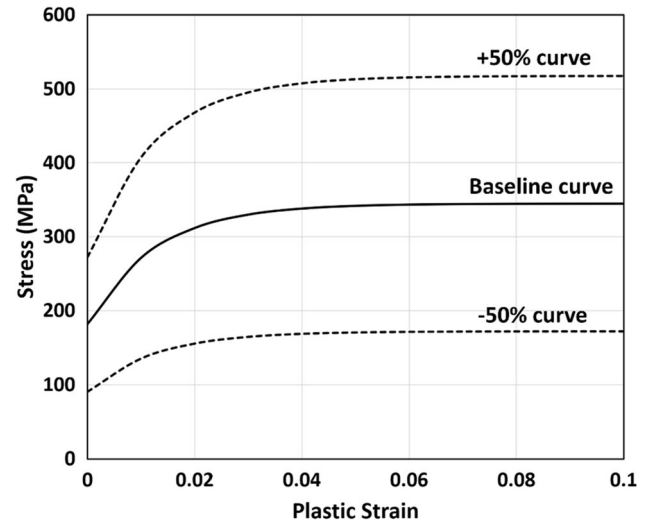

Fig. 2—Baseline flow curve of U-10Mo matrix material at 650 °C, and upper/lower bounds (*i.e.*, $\pm$ 50 pct) of random flow curves assigned to the multiple-grain model in Fig. 1.

including Young's modulus and Poisson's ratio, $\mathrm{d}\varepsilon_{kl}$ is total strain increment, $\mathrm{d}\varepsilon_{kl}^{e}$ is elastic strain increment, and $\mathrm{d}\varepsilon_{kl}^{p}$ is plastic strain increment. Using the classical theory of plasticity (the von Mises yield criterion and the associated flow rule), the plastic strain increment is obtained as shown in Eq. [2].

$$\mathrm{d}\varepsilon_{ij}^{p} = \frac{3}{2}\frac{\mathrm{d}\varepsilon_{p}^{eq}}{\sigma^{eq}} S_{ij}. \qquad [2]$$

Here, σ^{eq} and $\mathrm{d}\varepsilon_{p}^{eq}$ are the effective von Mises stress and the equivalent plastic strain increment, respectively, which are defined as follows:

$$\sigma^{eq} = \sqrt{\frac{3}{2} S_{ij}S_{ij}} \qquad [3]$$

$$d\varepsilon_p^{eq} = \sqrt{\frac{2}{3} d\varepsilon_{ij}^p d\varepsilon_{ij}^p}. \qquad [4]$$

Here, the S_{ij} terms constitute the deviatoric stress tensor. After each rolling simulation was completed, the strain fields at different levels of rolling reduction were used to estimate the deformation energy and then provided as input for subsequent annealing simulation based on the Potts model. The deformation energy was assumed to be a function of the total von Mises equivalent plastic strain, ε^{VM} ($= \int d\varepsilon_p^{eq}$). This equivalent plastic strain is calculated at the center of each element.

After a stage of recrystallization simulation is complete, the evolved microstructure is remeshed in such a way that each element remains the same size as in the initial FE model (i.e., 2×2 μm^2), and the resulting data are used for the next iteration of FEM rolling simulation. In these cases, recrystallized regions of the microstructure are assumed to be free of dislocations and strain. Therefore, the strain fields for the recrystallized regions are set to zero. For unrecrystallized regions, the remaining strain is carried over, and the total deformation energy is calculated by adding the deformation energy accumulated from the previous rolling steps to that created by the current round of rolling. This process is repeated until the target rolling reduction is reached. Note again that the polycrystalline anisotropic effects due to different grain orientations in the initial and recrystallized microstructures are considered in this study by adopting an independent flow curve for each grain.

This FEM modeling approach therefore can account for the variations of strain within the U-10Mo grain structure and the changes in grain shape due to hot rolling. Figure 3, for example, shows that after a 50 pct hot rolling treatment of the microstructure shown in Figure 1, the original grain structure has considerably elongated grains.

B. KMC Simulation of Recrystallization and Grain Growth

The Potts model of grain growth has been described in multiple publications over the course of several decades.[61–63] To incorporate recrystallization, the Potts model energy function must consider the local energetics associated with the nucleation and growth of recrystallized nuclei. Most models calculate the driving force for recrystallization as a function of the local strain, the components of which can be used to calculate the line densities of different types of dislocations.[21,27,41] Our
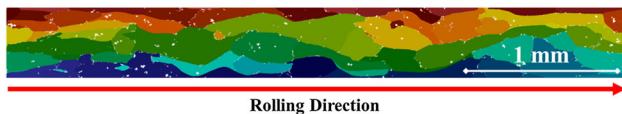

Rolling Direction

Fig. 3—An example longitudinal cross section of a 50 pct hot-rolled U-10Mo microstructure before recrystallization, with grain colors adjusted to emphasize the elongation of the deformed grains. Second-phase particles in the Potts model appear in white (Color figure online).

approach will calculate the driving force for recrystallization simply as a function of strain. To accomplish this, the Potts model energy function was modified:

$$E_i = U(\varepsilon_i^{VM}) + l^2 \sum_{j=0}^{NN} \gamma_{ij}(1 - \delta_{s_i s_j}). \qquad [5]$$

Here, the total energy of site i, E_i, is the sum of the nearest-neighbor interaction energies, γ_{ij} is the grain boundary energy between the grain IDs (i.e., s_i and s_j) of cell i and neighboring cell j. NN is the number of nearest neighbors, δ is the Kronecker delta, and the energy from accumulated strain ε_i^{VM} is referred to as U. Similar energy functions have been used for Potts model simulations of recrystallization in numerous previous instances.[25,27,29,55,63–67] U scales linearly with strain in the following form:

$$U = l^3 \frac{\sigma_Y \varepsilon_i^{VM}}{\beta}. \qquad [6]$$

Here, σ_Y is the yield strength of U-10Mo at room temperature and l is the cell width. A factor β accounts for the elimination of dislocation density through recovery before annealing and is assumed to be uniform for the entire material. A similar modification was previously used by Steiner et al. for the purpose of recrystallization simulation of rolled α-U, which is done so that both the deformation energy and grain boundary energy have commensurate units.[29] To account for effects such as temperature, driving force, and misorientation anisotropy, an equation for the Potts model switching probability as a function of the change in energy associated with the reorientation $p_{ij}(\Delta E)$ from the orientation of cell i to that of neighbor j was used:

$$p_{ij}(\Delta E) = \begin{cases} \frac{M_{ij}\gamma_{ij}}{M_{max}\gamma_{max}} & \Delta E \leq 0 \\ \frac{M_{ij}\gamma_{ij}}{M_{max}\gamma_{max}} e^{\frac{-\Delta E}{T_s}} & \Delta E > 0 \end{cases} \qquad [7]$$

Here, M_{ij} is the grain boundary mobility associated with a boundary between grains in cells i and j, γ_{ij} is the grain boundary energy between the same two grains, and ΔE is the change in energy associated with the reorientation. This function can therefore be used to calculate the probability of reorientations induced by (a) the curvature-driven growth of grains, (b) the growth of strain-free recrystallized grains, and (c) the nucleation of strain-free recrystallized grains, to which we will assign the term p_{rex}. Note that in this work, for simplicity, we have assumed that the grain boundaries have isotropic grain boundary energy and mobility as a function of misorientation. Simulations are performed this way because previous experimental work found that, while the process of hot rolling yielded prominent α and γ fibers, subsequent annealing generated random textures, which suggests that the nucleated recrystallized grains have nearly random orientations.[68] Therefore, for all simulations we have assumed $\gamma_{ij} = \gamma = 1.0$ J/m^2. The simulation temperature, T_S, frequently referred to as "$k_B T$," prevents the grain boundaries from pinning on

the simulation lattice.[69] The terms M_{Max} and γ_{Max} are the maximum allowed grain boundary mobility and energy, which we include to normalize the switching probability.

Kinetic Monte Carlo implementations of the Potts model are performed by calculating the probability of each possible reorientation within the microstructure, compiling the probabilities into a list, and calculating their sum, known as the "activity" of the system a_{tot}. Reorientations are then selected, rejection-free, by selecting a random number between zero and a_{tot} and searching the list of possible reorientations; this can be performed with $O(\ln(N))$ efficiency,[63] where N is the number of cells in the microstructure. Therefore, we express a_{tot} as follows:

$$a_{tot} = \sum_{i=1}^{N} a_i. \qquad [8]$$

To incorporate recrystallization reorientations, the equation for the activity of a cell a_i was modified to include not only the probability of reorientation to the orientation of one of the nearest neighbors p_j, but also the probability of reorientation to the orientation of a random recrystallized, strain-free grain ID, p_{rex}.

$$a_i = p_{rex} + \sum_{j}^{NN} p_j. \qquad [9]$$

By executing the KMC Potts model in this way, we can consider reorientations to the orientation of a specific recrystallized grain in the same way we consider reorientations to a nearest neighbor. This also allows us to consider recrystallization nucleation as a function of the energetic state of the microstructure, rather than allowing a set nucleation rate with a fixed nucleus size. Recrystallization nucleation events were forbidden in sites directly neighboring second-phase particles to prevent heterogeneous nucleation behavior in these locations. Using efficient search algorithms, reorientations can then be selected randomly, weighted by the activity of each reorientation, and converted to the equivalent number of Monte Carlo Steps (MCS) for the brute-force implementation.[62,63,70] The grain boundary mobility can be expressed as follows:

$$M_{ij} = \begin{cases} e^{\frac{-Q_{GG}}{RT}} & \text{Grain Growth} \\ \dfrac{e^{\frac{-Q_{Rex}}{RT}}}{B} & \text{Recrystallization} \end{cases} \qquad [10]$$

Here, Q_{GG} is the activation energy for grain growth, Q_{Rex} is the activation energy for recrystallization, R is the universal gas constant, and β is a fitting term that accounts for differences in simulated recrystallization and grain growth time scales. The values of Q_{GG} and Q_{Rex} were obtained through previous experimental work.[10] Based on Eq. [10] and the values for terms listed in Table I, the term M_{Max} from Eq. [7] can be defined as $M_{Max} = e^{-Q_{GG}/RT_{Max}}$, the mobility of a grain growth reorientation at $T = T_{Max}$. The value of β

Table I. Potts Model Simulation Parameters

Model Parameter	Value	Citation
l	2.0 μm	
T_S	0.5	
Q_{GG}	172.4 kJ	[10]
Q_{Rex}	100.6 kJ	[71]
T_{max}	1403 K (1133 °C)	
T	873–973 K (600 °C to 700 °C)	
β	25.3	
β	7.77×10^5	
σ_Y	35 MPa (700 °C)	[75]

can be determined through preliminary simulations comparing the time scales of grain growth and recrystallization.

The kinetics of recrystallization in U-10Mo were previously reported by Frazier et al. for 50 pct cold-rolled specimens annealed at 600 °C and 700 °C.[71] The experimental data were used to estimate the approximate annealing time necessary to reach 50 pct recrystallization and thereby extract the activation energy of U-10Mo recrystallization used for this work, 100.6 kJ/mole. In separate work, Frazier et al. also reported the Q_{GG} and grain growth constant k_0 of grain growth in U-10Mo for $n = 2$ grain growth behavior, i.e., 172.4 kJ/mole and 7.66×10^{-6} m²/s, respectively.[10] Note that $n = 2$ grain growth kinetics can be described as a function of temperature T and time as follows:

$$\overline{d}^2 - \overline{d}_0^2 = k_0 t e^{-Q_{GG}/RT}. \qquad [11]$$

Here, $\overline{d}$ represents the average grain diameter and $\overline{d}_0$ the initial average grain diameter. It is generally understood that, at an appropriate Monte Carlo simulation temperature T_S, Potts model simulations of isotropic, curvature-driven grain growth closely reflect $n = 2$ grain growth behavior.[69] Therefore, for a given Potts model simulation of isotropic U-10Mo grain growth, we can use an empirically calculated k_{Potts} to determine the number of MCS necessary for the Potts model to capture the equivalent period of annealing at a given temperature, t_{Potts}:

$$t_{Potts} = \frac{t k_0 e^{-Q_{GG}/RT}}{k_{Potts}}. \qquad [12]$$

Also, for the Potts model to correctly capture U-10Mo recrystallization behavior, the mobility of recrystallization reorientations in simulation must be modified so that the appropriate amount of recrystallization occurs for a given period at temperature. This can be accomplished by modifying the reorientation mobility by a factor B as described in Eq. [10]. The term B can be expressed in terms of the number of Monte Carlo steps required to reach the point of 50 pct recrystallization, $t_{Potts,0.5}$ and the number of Monte Carlo steps required to simulate a given time at temperature as calculated through Eq. [12]. Very simply,
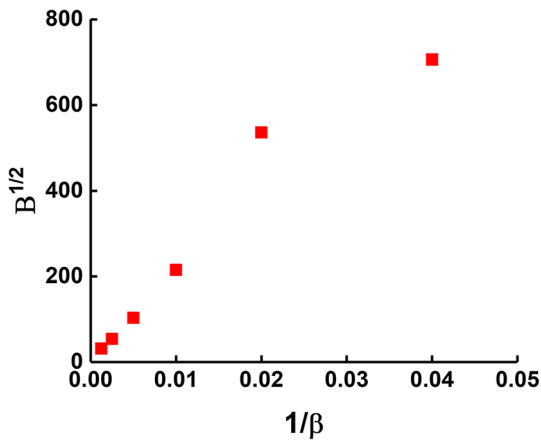
Fig. 4—The relationship between β and B, as calculated for a 50 pct cold rolled U-10Mo microstructure after 700 °C isothermal anneal.
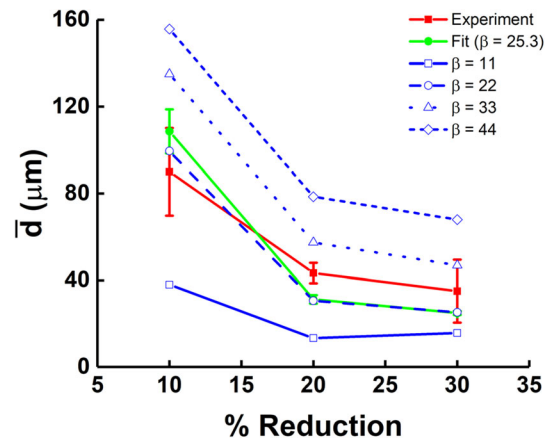

Fig. 5—Average grain size predicted by the Potts model for U-10Mo cold rolled to 10, 20, and 30 pct reductions after subsequent 2 hours of annealing at 700 °C.

$$B = \frac{t_{\text{Potts}}}{t_{\text{Potts},0.5}(\beta)}. \qquad [13]$$

Therefore, the term B is greater than unity when preliminary runs of the Potts model predict more rapid recrystallization than expected for a given period, and is less than unity if this recrystallization is slower than expected. It is important to mention that the term β was expected to significantly influence the recrystallization kinetics, since β controls the amount of driving force present to drive recrystallization. Therefore, the calculation of β and B is directly related to each other.

Using the previous work of Frazier et al.,[71–74] it was possible to perform preliminary FEM simulations as we have described to predict the mechanical response of U-10Mo to 50 pct cold-rolling reductions on a microstructure of similar average grain size, shown in Figures 1 and 6. By then simulating recrystallization with the Potts model, it was possible to calculate B as a function of β. Specifically, Potts model simulations were performed for recrystallization to match the conditions from Frazier et al.,[71] which found that for a 50 pct cold-rolling reduction on an approximately 25 μm U-10Mo grain structure, 50 pct recrystallization was achieved after approximately 84.28 minutes at 600 °C and after 20.28 minutes at 700 °C. For each β, the amount of MCS required to reach 50 pct recrystallization was recorded for both annealing temperatures to estimate $t_{\text{Potts},0.5}$. Isotropic simulations of grain growth were then performed to obtain estimations for k_{Potts}. Plots of B as a function of β can be found in Figure 4 and show that $B^{1/2}$ has an approximately inversely proportional linear relationship with β.

Next, we selected a value of β, which we used to calculate B for our model. This was done using grain size data from Kalia et al., who analyzed grain size changes for U-10Mo microstructures cold rolled to reductions of 10, 20, and 30 pct after a subsequent 2 hours of annealing at 700 °C. From these data, several preliminary simulations of rolling and recrystallization on our starting microstructure were run for different values of β, using the same rolling reduction and 2 hours of annealing at 700 °C. Using these results, the value for β that minimized the sum of the squared error with respect to the experimental data from Kalia et al. was calculated[72,74] and yielded $\beta = 25.3$. The quality of this fit can be shown in terms of the experimental data from Kalia et al. in Figure 5. It is clear from this plot that our methodology somewhat underestimates the U-10Mo grain size for recrystallization after larger reductions (20 and 30 pct) and somewhat overestimates the U-10Mo grain size for recrystallization after smaller (10 pct) reductions. Table I shows the values of the parameters described we used in our simulations.

C. Experimental

To investigate the effect of repeated hot rolling and annealing on the U-10Mo microstructure, four samples were initially cast and homogenized at 900 °C for 48 hours, resulting in a spheroidized carbide structure. Electron backscatter diffraction was used to capture a 2,040 μm wide and 916 μm thick image of the grain structure and particle locations. A representative microstructure of these samples can be seen in Figure 6.

All samples were then hot rolled at 650 °C. These four hot-rolled samples were subjected to 15 pct reduction passes, resulting in total reduction of 60 pct. Between all passes, an intermediate anneal was performed for 20 minutes at 700 °C. All samples were air cooled upon rolling. Sample microstructures were examined after rolling, but before intermediate annealing. The sample names were assigned as shown in Table II.

All samples were hand polished using standard metallographic procedures to a final polish of 0.05 μm colloidal silica solution on a low-nap pad. Since oxidation occurs readily, the samples were stored under vacuum at all times other than during polishing. Electron backscatter diffraction control parameters play a crucial role in finding patterns. The best parameters for these specimens were 30 keV with a large spot size (probe current) and medium magnification range on a Schottky-source field emission scanning electron
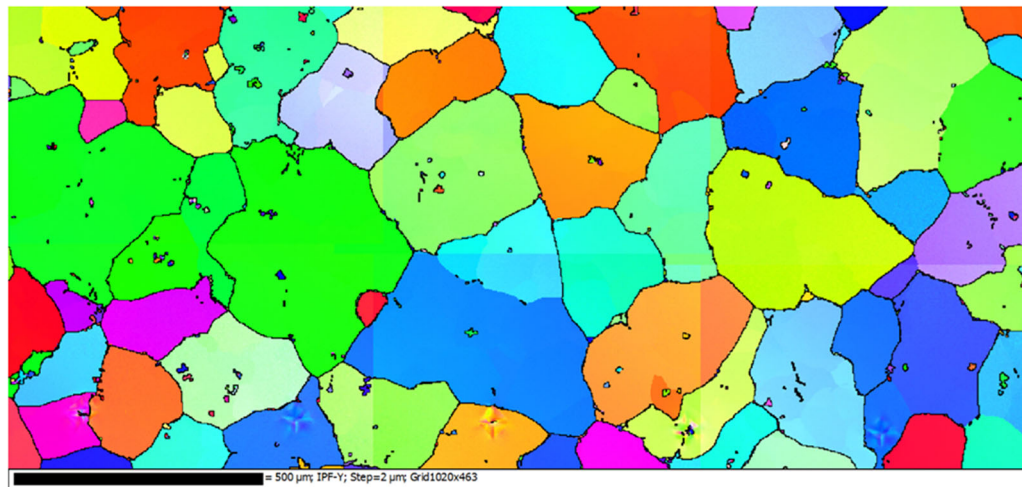
Rolling Direction

Fig. 6—The initial U-10Mo microstructure, as captured by an EBSD montage of a longitudinal cross section of the starting material.

Table II. Sample Names and Treatments

Sample Name	Number of Rolling Passes	Total Reduction (Percent)	Number of Intermediate Anneals
1 Pass	1	15	0
2 Pass	2	30	1
3 Pass	3	45	2
4 Pass	4	60	3

microscope. Diffuse patterns occur with heavily oxidized surfaces or at a lower keV or probe current.

Measurements were made over a regular hexagonal grid using a step size of one micrometer with a goal of including 1000 grains or more, where possible. For large-grained specimens, viewing windows showed too few grains to obtain statistically reliable texture measurements. The complete area scanned for EBSD analysis was approximately 3×1 mm^2 for all samples. Step size taken was 1 μm and all orientation maps were indexed as γ-U phase, whereas the black spots in the maps are either the traces of second-phase particles or points with confidence index < 0.1. As shown in Figure 6, the second-phase particles were indexed as UC and, in total, the average area fraction is around 0.03 as per EBSD image analysis.

The KAM was calculated for each captured microstructure. KAM as a quantitative value is used to characterize the distribution of dislocation density,[76,77] specifically, the geometrically necessary dislocations in the microstructure. The KAM value in this work is calculated using a misorientation definition of less than 5 deg and with respect to the third nearest neighbors.

The static recrystallization kinetics of hot-rolled U-10Mo were also observed experimentally. To accomplish this, rolled foils were prepared from an alloy of depleted U and 10.4 wt pct Mo. Cold rolling was performed on a Stanat model TA-215 two-high mill that was later converted to a four-high mill for cold-rolling operations to attain the desired foil thickness. In the two-high configuration, the top and bottom rolls were 4 in. in diameter and roughly 8 in. wide; in the four-high mill configuration, the 7/8 in. rolls were backed with 4 in. rolls. The rolling experiments were performed without lubrication. For rolling, the U-10Mo samples were wrapped in zirconium foils roughly 0.001-in. (0.025 mm) thick as a diffusion barrier. The mill was operated at 25 revolutions per minute and had a maximum load separation force of 100,000 lb. The samples were preheated in air at 700 °C for 20 to 30 minutes in a Thermcraft Model 1134 tube furnace before each pass and then hot rolled from 0.2 in. (5.08 mm) to 0.04 in. (1.02 mm), with 15 pct reductions per pass. The rolling occurred within 5 seconds of preheating to minimize heat loss during the hot rolling. This constitutes a total 80 pct reduction over several annealing and rolling steps. The progress of recrystallization of the as-rolled foil was quantitatively evaluated for each sample in EBSD using the procedure discussed by Frazier et al.[71] The resulting measurements will allow us to demonstrate whether our model accurately reproduces the expected U-10Mo recrystallization kinetics.

III. RESULTS

Simulations of this microstructure assumed an annealing temperature of 600 °C or 700 °C and a lattice resolution of 2 μm. Several FEM simulations were performed. First, FEM simulations were performed for 15 pct rolling passes, after which the KMC Potts model was used to simulate 20 minutes of annealing at 700 °C. These reduction percentages and annealing

times were selected to reproduce the recrystallization behavior observed experimentally in multiple passes of rolling U-10Mo for the same reduction, temperature, and duration. After each reduction, strain in the simulated recrystallized microstructure was removed, with the additional strain from the deformed sections of the microstructure allowed to remain. To prevent "single pixel" grains in deformation simulation, at the end of each Potts model simulation, deformed grains with fewer than four neighbors were removed from the microstructure, as if they had been absorbed by their neighboring grains. The resultant microstructure was then simulated for deformation and recrystallization response to additional rolling passes in the same way as before, with a reduction of up to 45 pct of the original thickness. Finally, two additional sets of rolling and recrystallization simulations were performed to evaluate the recrystallization kinetics after 80 pct total deformation, to allow us to compare recrystallization kinetics to the experimentally observed behavior. These simulations were expected to verify the applicability of our simulation approach to recrystallization after multiple passes of hot rolling.

A. Effect of Rolling and Intermediate Annealing on the Microstructure Development

The progress of recrystallization of the same U-10Mo microstructure for multiple iterations of rolling and annealing simulations along the longitudinal direction can be seen in Figure 7. These results are based on the three stages of 15 pct rolling passes and 20 minutes of intermediate anneals at the rolling temperature of 700 °C. Additionally, we can see the micrographs of U-10Mo with the equivalent treatments, plus a 15 pct final rolling step, in Figure 7. Qualitatively, the microstructures are very similar in that the grain size, grain size distribution, and spatial distribution of the grains are all very similar. At 30 pct deformation, populations of small, recrystallized grains appear to form along bands that had been highly deformed, while some recrystallized grains nucleate on grain boundaries or close to particles within the grains, which indicates that PSN is occurring. At 45 pct deformation, the recrystallized grains are considerably more numerous and are in the process of engulfing the larger grains from the initial deformed microstructure. Some areas in which PSN has occurred are still visible. At 60 pct deformation, it is difficult to distinguish the effect of PSN by visual inspection, because the recrystallized grains have almost entirely engulfed the initial microstructure. However, some of the larger deformed grains from the initial microstructure are still present.

Magnified portions of these micrographs are included to emphasize agreement between experiment and simulation in terms of the occurrence of PSN and the formation of recrystallized grains along deformation bands. Figure 8 shows a magnified image of the 30 pct rolled U-10Mo microstructure and the corresponding simulation using FEM and the Potts model. Figure 9 shows the simulated deformed microstructure and strain for each 15 pct rolling pass up to 60 pct reduction. This
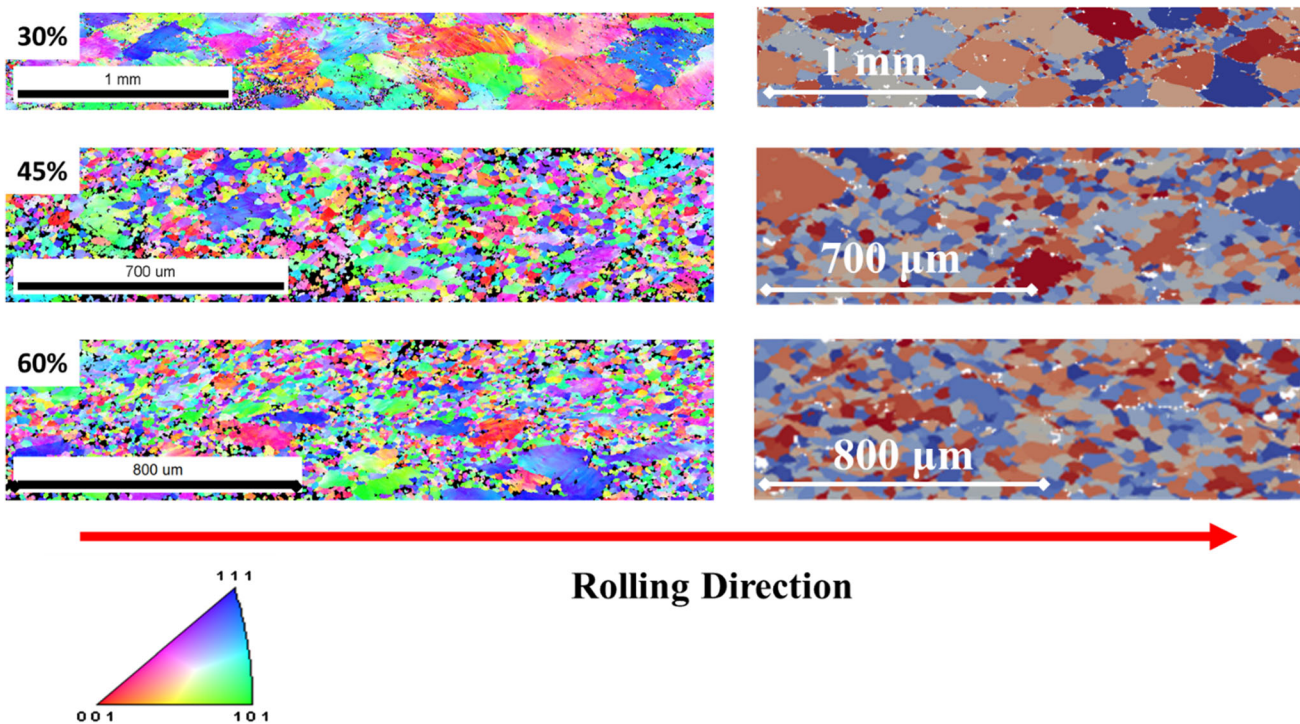

Fig. 7—Longitudinal cross section of the U-10Mo microstructure after two (30 pct), three (45 pct), and four (60 pct) hot rolling passes with 20 minutes of intermediate anneals at 700 °C, as observed experimentally with IPF EBSD images (left), and in Potts model simulation (right). In the EBSD images, regions in which a pattern could not be obtained are shown in black. In the Potts model simulation images, second-phase particles appear in white.
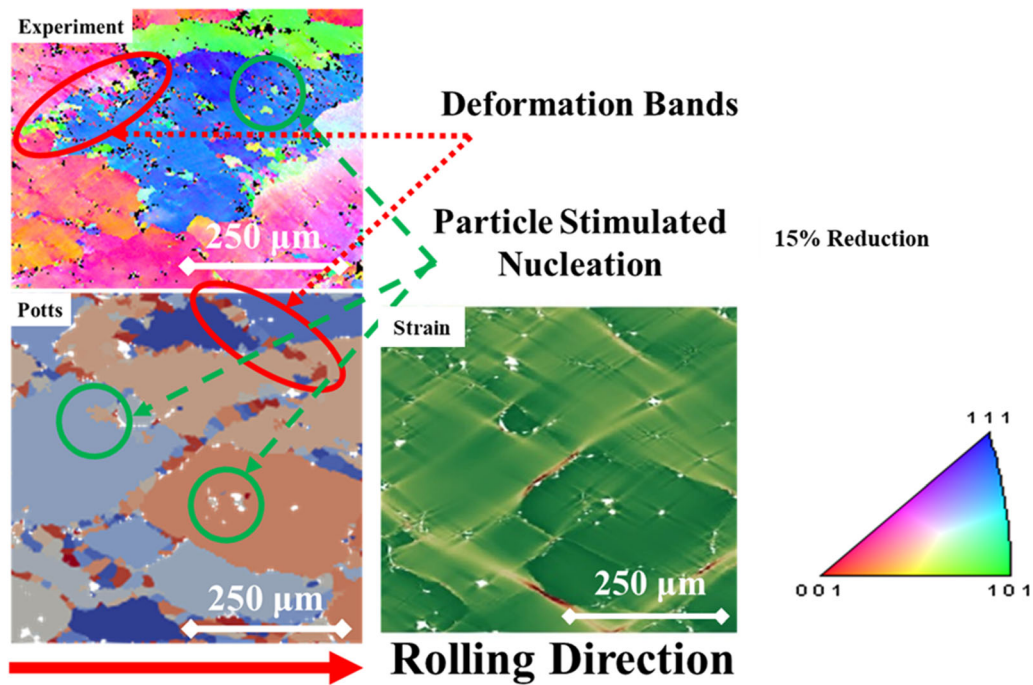
Fig. 8—Magnified longitudinal cross sections of U-10Mo microstructures after two (30 pct) hot-rolling passes with 20 minutes of intermediate anneals at 700 °C, as observed experimentally with IPF EBSD images (top), and in Potts model simulation (bottom). The associated distribution of strain predicted by FEM (bottom right) shows higher strain near UC particles. In the EBSD image, regions in which a pattern could not be obtained are shown in black. In the Potts model, UC particles appear in white. Selected regions containing recrystallization along highly deformed bands are circled in red, and selected regions in which PSN has occurred are circled in green (Color figure online).

shows that bands with high levels of strain become thinner with additional rolling passes. The fine, previously recrystallized grains in these microstructures have accumulated less strain than the larger grains from the initial structure.

These simulations can be compared with our experimental analysis of the hot-rolled microstructures, which are shown with KAM in Figure 10. Qualitatively, the micrographs are very similar to our FEM analysis. At 15 pct reduction, most of the strain accumulates either in bands or along grain boundaries, which is indicated by a higher KAM. At larger reductions, strain increasingly accumulates around the fine, more recently recrystallized microstructure. The more recently recrystallized grains appear to have smaller KAMs, which indicates lower dislocation density.

It is important to emphasize the limitations of KAM measurements in quantifying the distribution of dislocation density in microstructures. KAM measurements are sensitive to scan parameters such as step size. Therefore, KAM can only compare different regions of a single microstructure or different sample treatments using the same scan parameters, but reliably making other comparisons is difficult. Since KAM can only be used to calculate the density of geometrically necessary dislocations, it is difficult to compare our measurements to those for equivalent strain, from which we have calculated the driving force for recrystallization. A similar analog for dislocation density is grain orientation spread (GOS), which measures the variation in the

orientation within a grain from the average misorientation.[78] A plot of the cumulative GOS from the experimental data vs the cumulative strain from the FEM simulations is shown in Figure 11, in which we equate 1 deg of GOS with 2.88 pct strain. While this conversion is arbitrary, the trends observed in FEM are similar to those from experimental observations. Experimentally, the GOS increases after the first pass, and then decreases in the third and fourth passes. In the simulation, the strain similarly increases after the first pass, but decreases in the third and fourth passes. This pattern reflects the increase in dislocation density as dislocations are added to the U-10Mo microstructure with additional hot work and removed as recrystallization occurs during the intermediate anneals. Both simulation and experiment show that much of the stored dislocation density is not removed from the microstructure until after the second rolling pass. It is interesting that FEM predicts that the third and fourth passes of hot rolling should result in additional high strain regions, while none of these are observed in experiment in terms of GOS. This may be because the GOS can only reflect the density of geometrically necessary dislocations, and therefore likely underestimates the overall dislocation density.

However, it is important to point out that a high GOS indicates a high dislocation density, but like KAM, is difficult to directly relate GOS to dislocation density. To make such a quantitative comparison, we would need to
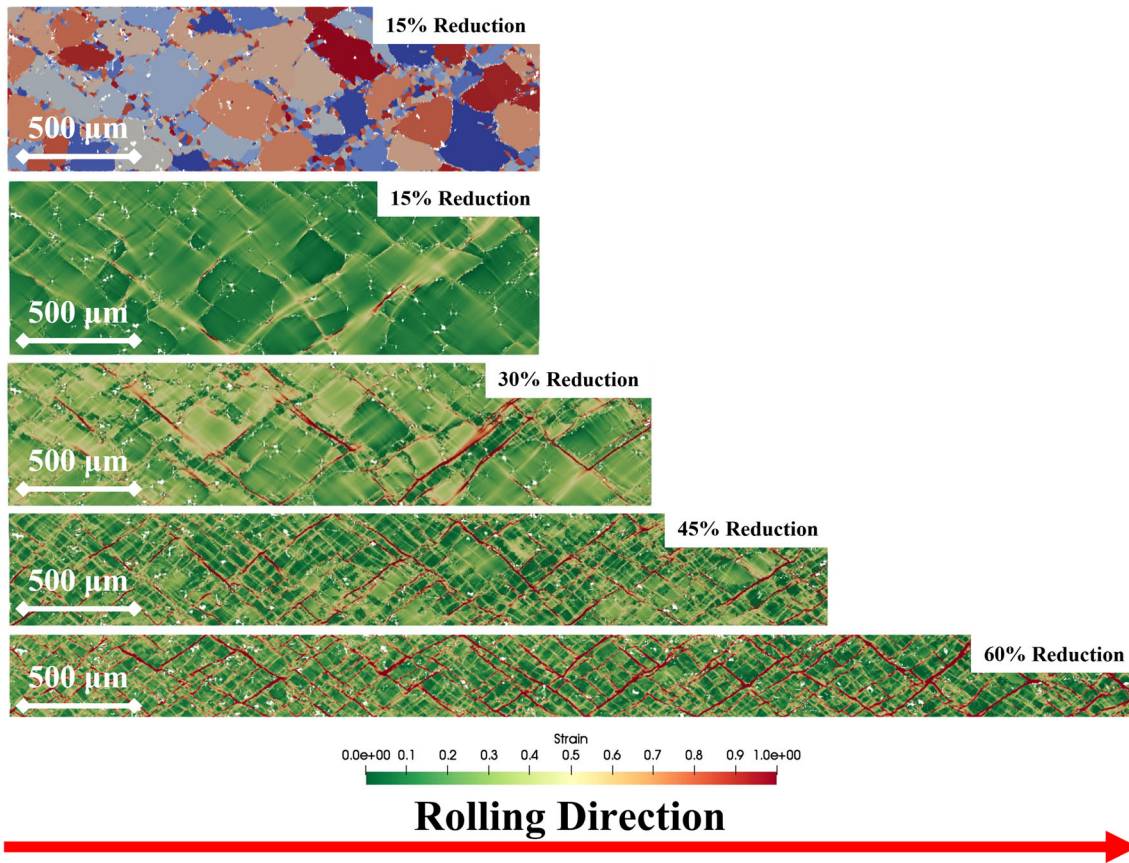
Fig. 9—The strain distribution within U-10Mo longitudinal cross sections for simulated hot-rolling reductions of 15, 30, 45, and 60 pct with intermediate annealing steps of 20 minutes at 700 °C. Second-phase particles are shown in white.
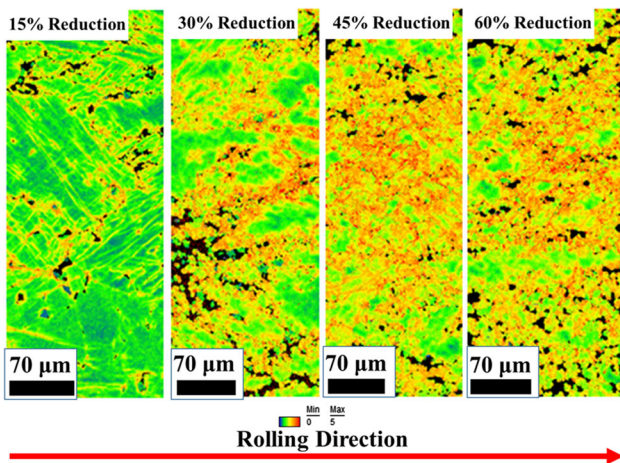

Fig. 10—The KAM maps of all samples calculated within misorientation of 5 deg with respect to third neighbors, collected from longitudinal U-10Mo cross sections for one, two, three, and four passes of hot rolling at 650 °C with intermediate 20 minutes of anneals at 700 °C. Areas where a pattern was not captured are shown in black.

Fig. 11—Cumulative distribution of the strain as calculated by FEM simulations of the first four passes of hot rolling, along with the cumulative distributions of GOS as observed in U-10Mo for the first four passes of hot rolling *via* EBSD. For the purpose of this figure, 1 deg of GOS is equated with 2.88 pct strain. Please note that this conversion is arbitrary.

implement another method of measuring dislocation density. However, these maps are nonetheless useful for identifying these types of qualitative trends.

B. Effect of Annealing on the Microstructure Development

The progress over 1 hour of recrystallization as simulated by the Potts model for U-10Mo for a 78 pct total rolling reduction over five hot-rolling passes with final annealing treatments of 600 °C and 700 °C can be seen in Figure 12. The graph shows that our simulations somewhat underestimate the rate of recrystallization within hot-rolled U-10Mo relative to the equivalent experimental treatment. To provide context to the discrepancy, when we assume that the U-10Mo foil is 0 pct recrystallized at the beginning of the final anneal, we can estimate using a point-by-point interpolation of the experimental measurements that the foil reaches 50 pct recrystallization after 21.1 minutes at 600 °C and after 5.3 minutes at 700 °C. From this, we can calculate an activation energy of recrystallization of $Q_{Rex} = 97.8$ kJ/mole. Similarly, we can estimate from our simulations that the U-10Mo foil reaches 50 pct recrystallization after 26.5 minutes at 600 °C and after 6.1 minutes at 700 °C, which translates to an effective $Q_{Rex} = 104.2$ kJ/mole. Both our estimate from these simulations and that from the experimental data are well within the margin of uncertainty from Frazier et al., who estimated $Q_{Rex} = 100.6 \pm 23.1$ kJ/mole on cold-rolled specimens. In this context, our simulations have captured the temperature-dependent recrystallization kinetics reasonably well.

Comparisons of the simulated and experimental grain size distributions after each set of rolling and annealing are shown in Figures 13(a) through (d) using the area fractions of grains. The distributions of recrystallized grain size from the simulation are also in reasonable agreement with experiment. Figure 13(d) shows that the average grain size falls precipitously from the initial average pre-rolling grain size of close to 150 μm to an average of 5 to 13 μm through progressive rolling and annealing steps. The standard deviation in the grain size distribution is also similar between experiment and simulation, as can be seen in Figure 13. These changes in grain size distribution are consistent with the occurrence of recrystallization in the microstructure.

The simulated microstructure has a noticeably larger population of smaller grains, which occurs because at high driving forces, many segments of the deformed microstructure are isolated from their parent grains by extensive recrystallization, creating "island grains." Although these grains are removed for the purpose of simulating successive rolling steps in FEM, it is reasonable to account for them when determining grain size distribution. We can see from Figure 13 that for each pass of rolling, the fractions of the fine recrystallized grains from the model are in reasonable agreement with those from experiment. The upper tails of the grain size distributions also show fairly similar area fractions of large, deformed grains. Our simulations disagree with experiment somewhat at 45 and 60 pct reductions, for which the larger grains (larger than roughly 60 μm in diameter) represent a larger area fraction than at the 30 pct reduction level. It is very unlikely that deformed grains grew between hot rolling and annealing steps; it is
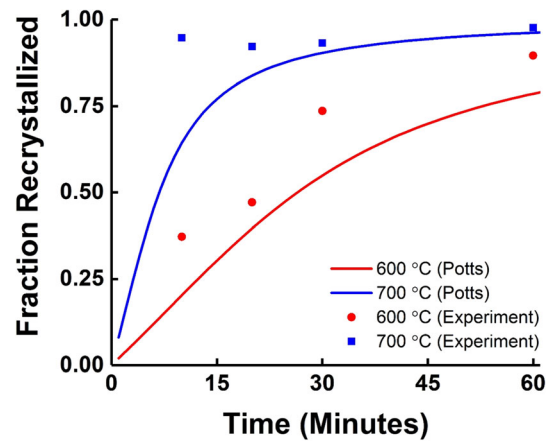

Fig. 12—Recrystallization progress (solid lines) of 78 pct hot-rolled U-10Mo at 600 °C and 700 °C, as predicted by the Potts model for five passes with 20 minutes of intermediate annealing at 700 °C. Experimentally observed data points for recrystallization progress of 80 pct hot-rolled U-10Mo are shown for comparison.

far more likely that this disagreement originates from variations in the recrystallization progress between different regions of the sample. These results indicate that our assumptions regarding the kinetics of grain growth and recrystallization are reasonable, as well as our assumptions with respect to the accumulated driving force for recrystallization vs strain.

IV. DISCUSSION

In thermomechanical processing, the purpose of recrystallization is to remove the dislocation density accumulated by forming and to produce a microstructure with suitable grain size, grain morphology, and texture. U-10Mo recrystallization and swelling under irradiation are believed to be sensitive to these features, so the fuel fabrication process must be improved to better control performance. It is therefore imperative that our simulations of U-10Mo deformation and annealing predict recrystallization and grain growth behaviors correctly. Recrystallization and grain growth behaviors are an important consideration for the fabrication of most alloys. As mentioned previously, to this end, numerous authors have simulated recrystallization response to deformation using integrated simulation methods.[18–21,24,29,30,40,44,50,51,79–83] Our method has the advantage that it can account for changes in grain shape with deformation. Although our approach cannot capture the entirety of the "pancaking" effect, which must also account for stress-induced grain boundary migration and grain rotation under strain, it does allow us to accurately predict the spatial distribution of second-phase particles in the deformed microstructure, which is an important consideration for simulating effects like PSN.[13]

It is notable that our nucleation algorithm allows recrystallized grains to nucleate via "wild" flips to random orientation IDs, which effectively assumes that the recrystallized grains have a critical nucleus size that they must reach to become stable in a stochastic process.
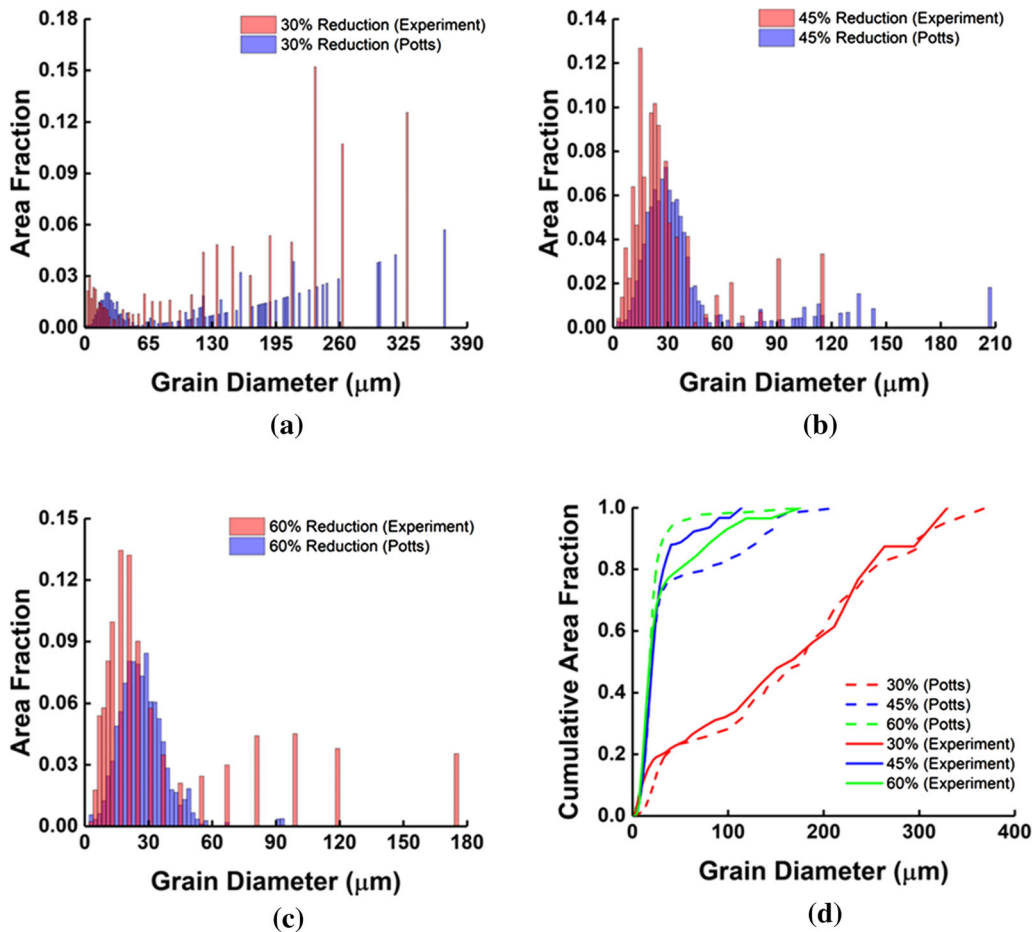
Fig. 13—Grain size distributions of U-10Mo for one to three passes of 15 pct rolling reduction plus 20 minutes of annealing at 700 °C, up to a total of 60 pct reduction in thickness and 60 minutes of annealing. (Note that grain size distributions are taken after the final 15 pct reduction before annealing). Size distributions are shown for (*a*) 30 pct, (*b*) 45 pct, and (*c*) 60 pct total reductions. Cumulative area fractions are shown in (*d*).

In most cases of recrystallization, the recrystallized grains form as a subgrain after the organization of dislocations during recovery, after which the boundaries migrate *via* a $V = MP$ relationship and the nucleus grows.[84] While our current simulations do not account for the formation of subgrains in the formation of recrystallized nuclei and do allow the shrinkage of recrystallized nuclei, we consider the assumed nucleus size of 2 μm for a wild flip as an acceptable break from understood behavior.

It is also important to consider the simulation's resolution with respect to the resolution of features smaller than second-phase particles in the microstructure. While our simulations have resolved the largest particles, which are known to have the largest effect in PSN,[13] smaller particles can have a considerable pinning effect that suppresses grain growth beyond a limiting grain size.[85–87] Many of these particles were observed to be on the order of tenths of micrometers in diameter,[10] so to account for this pinning effect observed in experiment, Potts model simulations of recrystallization must be performed at these higher resolutions where these fine particles can be incorporated. Resolving particles this fine while maintaining the

same field of view in our model would therefore require simulations roughly one hundred times more elements than that used for this work. However, it is important to point out that the periods of reheating simulated in this work are 20 minutes, while the periods required for Zener pinning to have a considerable effect on curvature-driven grain growth in U-10Mo are 1 to 4 hours.[10] Further, it is generally understood that particles with diameters less than approximately 0.5 μm do not cause PSN,[13] so FEM simulations of rolling may not need to resolve these particles. Therefore, for the purposes of the simulation in this work, it was deemed unnecessary to account for the fine UC particles within the U-10Mo microstructure.

Much of the recrystallization observed in these simulations clearly initiates at grain boundaries and nearby second-phase particles. This also occurs experimentally in U-10Mo during hot rolling. Recrystallization at these locations apparently occurs because the areas within the microstructure that experience the highest strain are regions close to grain boundaries and second-phase particles. As we pointed out previously, the surfaces of particles are forbidden as heterogeneous nucleation sites. However, the simulation allowed grain
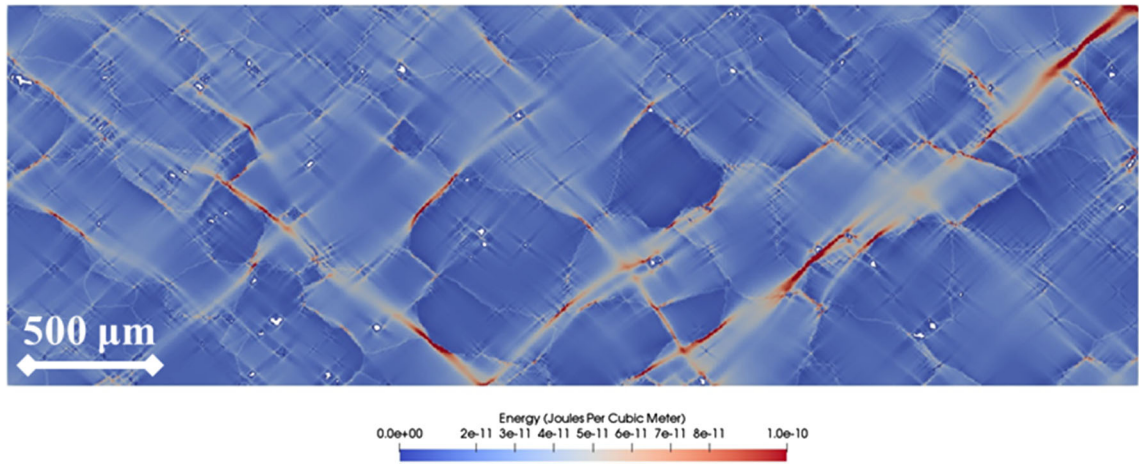
Fig. 14—The distribution of energetic states within the longitudinal cross section of the initial microstructure deformed to a 15 pct reduction in thickness. Regions with high energetic states form along the shear bands as a result of strain (red). Grain boundaries appear in light blue throughout the structure, which indicates that they have only a weak influence on recrystallization kinetics (Color figure online).

boundaries to become heterogeneous nucleation sites for recrystallized grains. It is believed that this effect does not have significant influence on recrystallization behavior because in most of the locations in which recrystallization occurs, the existing driving force is quite large. Therefore, the "necklace" microstructure does not form.[14] We can see this by evaluating the energetic state of each individual cell in the simulation, as shown in Figure 14 for a 15 pct rolling reduction on our initial captured microstructure. The grain boundaries can be seen outlining the original microstructure in a lighter blue. This indicates that nucleation is somewhat favored in these regions over the darker blue regions, but the highly strained regions, shown in red, are the most favored for recrystallization. Therefore, it is reasonable to argue that the influence of the grain boundaries on recrystallization nucleation is relatively small compared to the influence of localized strain.

Our model has several clear applications. The first is that it can predict the recrystallization behavior of a U-10Mo microstructure for a given rolling and annealing treatment. In this capacity, our simulations appear to reproduce the microstructural evolution seen in hot-rolled U-10Mo over several successive rolling passes, including changes in the grain size distribution, morphological features such as the locations of the nucleated recrystallized grains, and the overall recrystallization kinetics. Notably, our model predicts recrystallization that is slightly slower than was observed experimentally after a total hot-rolling reduction of 78 pct over five rolling and annealing passes, as shown in Figure 12. It is important to point out, however, that direct comparison to the experimental data on recrystallization progress is inexact. While in our Potts model simulations, nucleated recrystallized grains can be easily distinguished from the deformed regions of the microstructure, to make the same evaluation from EBSD maps, grains are classified as recrystallized by setting arbitrary cutoffs of grain average misorientation and GOS. Therefore, depending on these cutoffs, the

agreement of our model with the experimental data may vary somewhat.

The second application of our model is that it can evaluate the effects of individual microstructural features on the recrystallization and annealing behavior. For example, simply removing the particles from our U-10Mo microstructure can help reveal the effect of PSN on the overall recrystallization behavior and kinetics. This capability is not unique; other, similar methodologies have been developed to simulate the progress of PSN within a deformed microstructure. For example, Adam et al. studied PSN within aluminum alloy AA7050 using the Monte Carlo Potts model in two separate publications.[25,26] In these articles, EBSD maps of the microstructure were used as the initial state for the Monte Carlo simulations, and grain orientation measurements from these maps were used to simulate grain structure evolution. Somewhat similar to our work, Zhang et al. evaluated dynamic recrystallization in Inconel 718 as a function of temperature, strain rate, and the presence of δ phase within the microstructure using a cellular automata model and could accurately reproduce dynamic recrystallization behavior as a function of strain.[88] Sidor et al. could predict the evolution of texture within particle-containing Al alloys using an orientation selection algorithm.[89] The phenomenon of PSN has been studied in more general terms by other authors.[16,90,91] Alves et al., for example, used a causal cone method to validate an analytical solution for the effect of different volume fractions of second-phase particles on transformation processes.[91] However, to our knowledge, our work is the first application of this type of modeling that can study the influence of PSN within U-10Mo fuel foils over the entire rolling and annealing process. An analysis of the effects of PSN in U-10Mo that uses our model will be discussed in a future publication. Additionally, with simulation parameters adjusted to account for rolling temperature, the recrystallization behavior for different rolling temperatures can also be explored. This capability will be examined in future work.

V. CONCLUSIONS

An integrated model of U-10Mo rolling and annealing was constructed and implemented to simulate the recrystallization behavior of U-10Mo after each of several rolling passes at 700 °C. Recrystallization kinetics matched those observed experimentally for hot-rolled U-10Mo. These simulations reproduced the experimentally observed grain size distributions of U-10Mo between multiple hot rolling, 15 pct reduction passes to 60 pct reduction. Further study is required to determine the roles of the grain size, particle size, particle volume fraction, and spatial distribution on the effects of PSN on U-10Mo recrystallization, which will help predict superior fuel fabrication parameters.

DATA AVAILABILITY

The raw/processed data required to reproduce these findings cannot be shared at this time because it forms part of an ongoing study.

COMPETING INTERESTS

The authors declare that they have no known competing financial interests or personal relationships that could have appeared to influence the work reported in this paper.

OPEN ACCESS

REFERENCES

1. J. Jue, T.L. Trowbridge, C.R. Breckenridge, G.A. Moore, M.K. Meyer, and D.D. Keiser: *J. Nucl. Mater.*, 2015, vol. 460, pp. 153–59.
2. A.J. Clarke, K.D. Clarke, R.J. McCabe, C.T. Necker, P.A. Papin, R.D. Field, A.M. Kelly, T.J. Tucker, R.T. Forsyth, P.O. Dickerson, J.C. Foley, H. Swenson, R.M. Aikin, and D.E. Dombrowski: *J. Nucl. Mater.*, 2015, vol. 465, pp. 784–92.
3. S. Hu, V. Joshi, and C.A. Lavender: *J. Miner. Met. Mater. Soc.*, 2017, vol. 69, pp. 2554–562.
4. L. Liang, Z.G. Mei, Y.S. Kim, B. Ye, G. Hofman, M. Anitescu, and A.M. Yacout: *Comput. Mater. Sci.*, 2016, vol. 124, pp. 228–37.
5. L. Liang, Z.G. Mei, and A.M. Yacout: *Comput. Mater. Sci.*, 2017, vol. 138, pp. 16–26.
6. Z. Xu, V. Joshi, S. Hu, D. Paxton, C. Lavender, and D. Burkes: *J. Nucl. Mater.*, 2016, vol. 471, pp. 154–64.
7. W.E. Frazier, S. Hu, D.E. Burkes, and B.W. Beeler: *J. Nucl. Mater.*, 2019, vol. 524, pp. 164–76.
8. E.A. Nyberg, V.V. Joshi, C.A. Lavender, D.M. Paxton, and D.E. Burkes: *The Influence of Casting Conditions on the Microstructure of As-Cast U-10Mo Alloys: Characterization of the Casting Process Baseline.* PNNL-23049, Pacific Northwest National Laboratory, Richland, WA, 2013. https://doi.org/10.2172/1163444.
9. L. Li, A. Fortier, D.R. Tamayo, V.V. Joshi, and A. Soulami: *Mate. Today Commun.*, 2022, vol. 32, p. 103910.
10. W.E. Frazier, S. Hu, N. Overman, C. Lavender, and V.V. Joshi: *J. Nucl. Mater.*, 2018, vol. 498, pp. 254–58.
11. R.P. De Siqueira, H.R.Z. Sandim, and D. Raabe: *Metall. Mater. Trans. A*, 2013, vol. 44A, pp. 469–78.
12. W. Xu, M. Ferry, J.M. Cairney, and F.J. Humphreys: *Acta Mater.*, 2007, vol. 55, pp. 5157–167.
13. F.J. Humphreys and M. Hatherly: *Recrystallization and Related Annealing Phenomena*, 2nd ed., Elsevier Ltd., Oxford, 2004, pp. 287–304.
14. K. Huang and R.E. Logé: *Mater. Des.*, 2016, vol. 111, pp. 548–74. https://doi.org/10.1016/j.matdes.2016.09.012.
15. S.A. Humphry-Baker and C.A. Schuh: *J. Appl. Phys.*, 2014, vol. 116, p. 17305. https://doi.org/10.1063/1.4901235.
16. R.L. Goetz: *Scripta Mater.*, 2005, vol. 52, pp. 851–56.
17. F.J. Humphreys and P.N. Kalu: *Acta Metall.*, 1987, vol. 35, pp. 2815–829.
18. C. Zheng, N. Xiao, D. Li, and Y. Li: *Comput. Mater. Sci.*, 2008, vol. 44, pp. 507–14.
19. F. Chen, K. Qi, Z. Cui, and X. Lai: *Comput. Mater. Sci.*, 2014, vol. 83, pp. 331–40.
20. C. Haase, M. Kühbach, L.A. Barrales-Mora, S. Leen, F. Roters, D.A. Molodov, and G. Gottstein: *Acta Mater.*, 2015, https://doi.org/10.1016/j.actamat.2015.08.057.
21. D.K. Kim, W. Woo, W.W. Park, Y.T. Im, and A. Rollett: *Comput. Mater. Sci.*, 2017, vol. 129, pp. 55–65.
22. D. Raabe and L. Hantcherli: *Comput. Mater. Sci.*, 2005, https://doi.org/10.1016/j.commatsci.2004.12.067.
23. P. Zhao, T.S.E. Low, Y. Wang, and S.R. Niezgoda: *Int. J. Plast.*, 2016, vol. 80, pp. 38–55.
24. X. Li, X. Li, H. Zhou, X. Zhou, F. Li, and Q. Liu: *Comput. Mater. Sci.*, 2017, vol. 140, pp. 95–104. https://doi.org/10.1016/j.commatsci.2017.08.039.
25. K. Adam, J.M. Root, Z. Long, and D.P. Field: *J. Mater. Eng. Perform.*, 2017, vol. 26, pp. 207–13.
26. K.F. Adam, Z. Long, and D.P. Field: *Metall. Mater. Trans. A*, 2017, vol. 48A, pp. 2062–076.

27. K. Adam, D. Zöllner, and D.P. Field: *Model. Simul. Mater. Sci. Eng.*, 2018, vol. 26, p. 035011. https://doi.org/10.1088/1361-651X/aaa146.
28. Z.C. Sun, H.L. Wu, J. Cao, and Z.K. Yin: *Int. J. Plast.*, 2018, vol. 106, pp. 73–87. https://doi.org/10.1016/j.ijplas.2018.03.002.
29. M.A. Steiner, R.J. McCabe, E. Garlea, and S.R. Agnew: *J. Nucl. Mater.*, 2017, vol. 492, pp. 74–87. https://doi.org/10.1016/j.jnucmat.2017.04.026.
30. M.G. Llorens, A. Griera, P.D. Bons, R.A. Lebensohn, L.A. Evans, D. Jansen, and I. Weikusat: *Earth Planet. Sci. Lett.*, 2016, vol. 450, pp. 233–42. https://doi.org/10.1016/j.epsl.2016.06.045.
31. S.F. Li, J. Lind, C.M. Hefferan, R. Pokharel, U. Lienert, A.D. Rollett, and R.M. Suter: *J. Appl. Crystallogr.*, 2012, vol. 45, pp. 1098–108.
32. A. Cerrone, C. Stein, R. Pokharel, C. Hefferan, J. Lind, H. Tucker, R. Suter, A. Rollett, and A. Ingraffea: *Model. Simul. Mater. Sci. Eng.*, 2015, https://doi.org/10.1088/0965-0393/23/3/035006.
33. M. Zehetbauer, T. Ungár, R. Kral, A. Borbély, E. Schafler, B. Ortner, H. Amenitsch, and S. Bernstorff: *Acta Mater.*, 1999, vol. 47, pp. 1053–061.
34. A.C. Leff, C.R. Weinberger, and M.L. Taheri: *Ultramicroscopy*, 2015, vol. 153, pp. 9–21. https://doi.org/10.1016/j.ultramic.2015.02.002.
35. J. Jiang, T. Ben Britton, and A.J. Wilkinson: *Int. J. Plast.*, 2015, vol. 69, pp. 102–17.
36. P.D. Littlewood and A.J. Wilkinson: *Acta Mater.*, 2012, vol. 60, pp. 5516–525.
37. W.Z. Abuzaid, M.D. Sangid, J.D. Carroll, H. Sehitoglu, and J. Lambros: *J. Mech. Phys. Solids*, 2012, vol. 60, pp. 1201–220. https://doi.org/10.1016/j.jmps.2012.02.001.
38. D.B. Needleman, H. Choil, D.M. Powell, and T. Buonassisi: *Physica Status Solidi Rapid Res. Lett.*, 2013, vol. 7, pp. 1041–044. https://doi.org/10.1002/pssr.201308150.
39. S. Woo, M. Bertoni, K. Choi, S. Nam, S. Castellanos, D.M. Powell, T. Buonassisi, and H. Choi: *Sol. Energy Mater. Sol. Cells*, 2016, vol. 155, pp. 88–100. https://doi.org/10.1016/j.solmat.2016.03.040.
40. T. Takaki and Y. Tomita: *Int. J. Mech. Sci.*, 2010, vol. 52, pp. 320–28.
41. M. Jafari, M. Jamshidian, S. Ziaei-Rad, D. Raabe, and F. Roters: *Int. J. Plast.*, 2017, vol. 99, pp. 19–42.
42. H. Zhang, J. Liu, D. Sui, Z. Cui, and M.W. Fu: *Int. J. Plast.*, 2018, vol. 100, pp. 69–89. https://doi.org/10.1016/j.ijplas.2017.09.011.
43. F. Roters, P. Eisenlohr, L. Hantcherli, D.D. Tjahjanto, T.R. Bieler, and D. Raabe: *Acta Mater.*, 2010, vol. 58, pp. 1152–211.
44. T. Takaki, Y. Hisakuni, T. Hirouchi, A. Yamanaka, and Y. Tomita: *Multi-Phase-Field Simulations for Dynamic Recrystallization*, vol. 45, Elsevier B.V., Amsterdam, 2009.
45. X.H. Hu, D.S. Wilkinson, M. Jain, P.D. Wu, and R.K. Mishra: *Mater. Sci. Eng. A*, 2011, vol. 528, pp. 2002–016.
46. X. Hu, D.S. Wilkinson, M. Jain, and R.K. Mishra: *Int. J. Solids Struct.*, 2009, vol. 46, pp. 2650–658.
47. X. Hu, X. Wang, V.V. Joshi, and C.A. Lavender: *J. Nucl. Mater.*, 2018, vol. 500, pp. 270–79.
48. G. Cheng, X. Hu, W.E. Frazier, C.A. Lavender, and V.V. Joshi: *Mater. Sci. Eng. A*, 2018, vol. 736, pp. 41–52.
49. E. Miyoshi, T. Takaki, M. Ohno, Y. Shibuta, S. Sakane, T. Shimokawabe, and T. Aoki: *npj Comput. Mater.*, 2017, https://doi.org/10.1038/s41524-017-0029-8.
50. B. Scholtes, R. Boulais-Sinou, A. Settefrati, D. Pino, I. Poitrault, A. Montouchet, N. Bozzolo, and M. Bernacki: *Comput. Mater. Sci.*, 2016, vol. 122, pp. 57–71.
51. O. Beltran, K. Huang, and R.E. Logé: *Comput. Mater. Sci.*, 2015, vol. 102, pp. 293–303.
52. E.A. Holm, T.D. Hoffmann, A.D. Rollett, and C.G. Roberts: *IOP Conf. Ser.: Mater. Sci. Eng.*, 2015, vol. 89, p. 012005.
53. W. Frazier, C. Wang, Z. Xu, and N. Overman: *Metall. Mater. Trans. A*, 2020, vol. 51A, pp. 533–44.
54. P.E. Goins and E.A. Holm: *Comput. Mater. Sci.*, 2016, vol. 124, pp. 411–19.
55. G.B. Sarma, B. Radhakrishnan, and T. Zacharia: *Acta Mater.*, 1998, vol. 46, pp. 4415–433.
56. A.E. Dwight: *J. Nucl. Mater.*, 1960, vol. 2, pp. 81–7.
57. M. Tokar, A.W. Nutt, and J.A. Leary: Mechanical Properties of Carbide and Nitride Reactor Fuels, LA-4452, Los Alamos National Laboratory, Los Alamos, NM, 1970.
58. W. Frazier, C. Wang, Z. Xu, N. Overman, S. Hu, and V.V. Joshi: *Metall. Mater. Trans. A*, 2020, vol. 51A, pp. 533–44.
59. X.H. Hu, M. Jain, D.S. Wilkinson, and R.K. Mishra: *Acta Mater.*, 2008, vol. 56, pp. 3187–201.
60. J. Rest, Y.S. Kim, and G.L. Holmes: *U-Mo Fuels Handbook*, Version 1.0, Argonne National Laboratory, 2006.
61. S.A. Safran, P.S. Sahni, and G.S. Grest: *Phys. Rev. B*, 1983, vol. 28, pp. 2693–704.
62. E.A. Holm and G.N. Hassold: *Comput. Phys.*, 1993, vol. 7, pp. 97–207.
63. D. Raabe: *Acta Mater.*, 2000, vol. 48, pp. 1617–628.
64. A.D. Rollett, D.J. Srolovitz, M.P. Anderson, and R.D. Doherty: *Acta Metall. Mater.*, 1992, vol. 40, pp. 3475–495.
65. B.L. DeCost, H. Jain, A.D. Rollett, and E.A. Holm: *JOM*, 2017, vol. 69, pp. 456–65.
66. A. Rollett: *Prog. Mater. Sci.*, 1997, vol. 42, pp. 79–99.
67. A. Williamson and J. Delplanque: *Comput. Mater. Sci.*, 2016, vol. 124, pp. 114–29.
68. B.J. Schuessler, D.P. Field, N.R. Overman, and V.V. Joshi: *Metall. Mater. Trans. A*, 2021, vol. 52A, pp. 3871–879.
69. D. Zöllner: *Comput. Mater. Sci.*, 2014, vol. 86, pp. 99–107.
70. P.S. Sahni, D.J. Srolovitz, G.S. Grest, M.P. Anderson, and S.A. Safran: *Phys. Rev. B*, 1983, vol. 28, pp. 2705–716.
71. W.E. Frazier, S. Hu, N. Overman, R. Prabhakaran, C. Lavender, and V.V. Joshi: *J. Nucl. Mater.*, 2019, vol. 513, pp. 56–61.
72. K. Kalia, W.E. Frazier, D.P. Field, and V.V. Joshi: *Journal of Physics Conference Series*, IOP Publishing, Ghent, 2019.
73. J.I. Reeve, B.J. Schuessler, W.E. Frazier, D.P. Field, and V.V. Joshi: *J. Nucl. Mater.*, 2022, vol. 559, p. 153445. https://doi.org/10.1016/j.jnucmat.2021.153445.
74. K. Kalia: Masters Thesis, Washington State University, 2017.
75. C. Wang, A. Soulami, Z. Xu, G. Cheng, S. Hu, D. Burkes, W.E. Frazier, K.S. Choi, X. Wang, X. Hu, C.A. Lavender, and V.V. Joshi: *Process Modeling of U-10wt % Mo Alloys Using Integrated Computational Materials Engineering*, PNNL-28640, Pacific Northwest National Laboratory, Richland, WA, 2019.
76. C. Moussa, M. Bernacki, R. Besnard, and N. Bozzolo: *IOP Conf. Ser.: Mater. Sci. Eng.*, 2015, vol. 89, p. 012038.
77. M. Kamaya: *Ultramicroscopy*, 2011, vol. 111, pp. 1189–199.
78. P.O. Malta, D.S. Alves, A.O.V. Ferreira, I.D. Moutinho, C.A.P. Dias, and D.B. Santos: *Metall. Mater. Trans. A*, 2017, vol. 48A, pp. 1288–309.
79. Z. Jin and Z. Cui: *Comput. Mater. Sci.*, 2012, vol. 63, pp. 249–55.
80. M.S. Salehi and S. Serajzadeh: *Comput. Mater. Sci.*, 2012, vol. 53, pp. 145–52.
81. P. Zhao, T. Song En Low, Y. Wang, and S.R. Niezgoda: *Int. J. Plast.*, 2016, vol. 80, pp. 38–55.
82. L. Chen, J. Chen, R.A. Lebensohn, Y.Z. Ji, T.W. Heo, S. Bhattacharyya, K. Chang, S. Mathaudhu, Z.K. Liu, and L.Q. Chen: *Comput. Methods Appl. Mech. Eng.*, 2015, vol. 285, pp. 829–48.
83. M. Bernacki, R.E. Logé, and T. Coupez: *Scripta Mater.*, 2011, vol. 64, pp. 525–28.
84. P.R. Rios, F. Siciliano Jr., H.R.Z. Sandim, R.L. Plaut, and A.F. Padilha: *Mater. Res.*, 2005, vol. 8, pp. 225–38.
85. C.S. Smith: *Trans. Am. Inst. Min. Eng.*, 1948, vol. 175, pp. 15–51.
86. P.A. Manohar, M. Ferry, and T. Chandra: *ISIJ Int.*, 1998, vol. 38, pp. 913–24.
87. W.E. Frazier, S. Hu, N. Overman, C. Lavender, and V.V. Joshi: *J. Nucl. Mater.*, 2019, vol. 526, 151763.
88. F. Zhang, D. Liu, and Y. Yang: *Model. Simul. Mater. Sci. Eng.*, 2019, vol. 27, p. 035002.
89. J.J. Sidor, K. Decroos, R.H. Petrov, and L.A.I. Kestens: *Int. J. Plast.*, 2015, vol. 66, pp. 119–37.
90. E. Fjeldberg and K. Marthinsen: *Comput. Mater. Sci.*, 2010, vol. 48, pp. 267–81.
91. A.L.M. Alves, E. Villa, and P.R. Rios: *Acta Mater.*, 2017, vol. 131, pp. 523–33.